Bulletin of the Seismological Society of America, Vol. 96, No. 5, pp. 1753–1763, October 2006, doi: 10.1785/0120050253

Strain Green's Tensors, Reciprocity, and Their Applications to Seismic Source and Structure Studies

by Li Zhao, Po Chen, and Thomas H. Jordan

Abstract Green's function approach is widely used in modeling seismic waveform. The representation theorem expresses the wave field as the inner product of the moment tensor and the spatial gradients of the Green's tensor. Standard practice in waveform calculations has been to compute the Green's tensors first and then obtain their gradients by numerical differentiation. The reciprocity of the Green's tensor enables us to express the wave field explicitly in terms of the strain Green's tensor, a third-order tensor composed of the spatial gradients of the Green's tensor elements. We propose here to use the strain Green's tensors rather than the Green's tensors themselves in computing the waveforms. By bypassing the need for Green's tensors and directly using the strain Green's tensors, we can improve the computational efficiency in waveform modeling while eliminating the possible errors from numerical differentiation. The strain Green's tensor elements are also directly related to the partial derivatives of the waveforms with respect to moment tensor elements and structural parameters. Through the inversion of the focal mechanisms of 27 small events in the Los Angeles region, we demonstrate the effectiveness of the strain Green's tensor database approach in quickly recovering source parameters based on realistic 3D models. We show that the same database can also be used to improve the efficiency and accuracy in computing the Fréchet kernels for tomography inversions.

Introduction

Seismic waveforms of finite frequency carry a great deal of information on earthquake sources and earth structure. Successful and efficient waveform modeling in source and structural studies are important in ensuring the quality of measurements and are therefore instrumental in improving the resolution and reliability of the resulting source and structural models. Recent developments in both waveform modeling techniques and high-performance computational facilities have also helped seismologists to pursue the waveform approach at relatively short periods in ever more complex structural environments (e.g., Olsen, 1994; Graves, 1996; Komatitsch *et al.*, 2004). The applications of these accurate waveform-modeling methods have allowed the use of 3D reference models to be used in both source studies (Liu *et al.*, 2004; Chen *et al.*, 2005) and in constructing the sensitivity kernels (Zhao *et al.*, 2005; Q. Liu and J. Tromp, unpublished manuscript, 2006) for structural inversions.

Numerical waveform-modeling tools provide the wavefield solutions caused by earthquake sources that are either point or distributed moment tensors. They can also simulate the Green's functions, the wave fields from unit impulsive point forces that are also very useful in various kinds of waveform-based source and structural studies. Green's functions are particularly helpful in improving the computational efficiency when there is a need to calculate the waveforms for the same source-station pair again and again since they use the same Green's functions. Furthermore, when waveforms at the same station from multiple sources are needed, a joint use of the complete set of the Green's functions from the station, that is, the Green's tensor, and its reciprocity property can reduce the required computations even more drastically (Eisner and Clayton, 2001; Graves and Wald, 2001).

In calculating waveforms from earthquake sources described by moment tensors, it is in fact the spatial gradients of the Green's tensors that are directly used. Currently, the standard approach (Eisner and Clayton, 2001; Graves and Wald, 2001) obtains the Green's tensors from numerical simulations and then uses numerical differentiation to compute the spatial gradients of the Green's tensors. In the present study we extend this treatment and propose an approach in which we use the reciprocity and express the wave field explicitly in terms of the strain Green's tensors, a third-order tensor composed of the spatial gradients of the Green's tensor elements. By bypassing the need for the Green's tensors and their numerical differentiation, waveform calculation

becomes more efficient without any loss of the accuracy. In the following sections, we first discuss in brief the definition of strain Green's tensor and its relation to waveform through reciprocity. Then we present the examples for the applications of our approach in computing synthetic seismograms in 3D reference models, in earthquake source-parameter inversions, and in structural-sensitivity Fréchet kernel calculations.

Strain Green's Tensors

In seismology, the strain tensor is often used to describe the deformation of the earth medium caused by seismic-wave-generated displacement field and is linearly related to the stress field by the constitutive law. It is a second-order symmetric tensor defined in terms of the spatial-gradient elements of the displacement vector:

$$\boldsymbol{\varepsilon}(\mathbf{r},\, t) \;=\; \frac{1}{2}\left\{[\nabla \mathbf{u}(\mathbf{r},\, t)] \;+\; [\nabla \mathbf{u}(\mathbf{r},\, t)]^{\mathrm{T}}\right\}. \qquad (1)$$

Analogous to the definition in equation (1), we can form a third-order tensor by using the spatial-gradient elements of the second-order Green's tensor:

$$\mathbf{H}(\mathbf{r},\, t;\, \mathbf{r}_{\mathrm{S}}) \;=\; \frac{1}{2}\left\{[\nabla \mathbf{G}(\mathbf{r},\, t;\, \mathbf{r}_{\mathrm{S}})] \;+\; [\nabla \mathbf{G}(\mathbf{r},\, t;\, \mathbf{r}_{\mathrm{S}})]^{213}\right\}. \qquad (2)$$

In equation (2), $\mathbf{r}_{\mathrm{S}}$ is the source location of the Green's tensor, the spatial gradient operator acts on the field coordinate $\mathbf{r}$, and the notation $[\cdot]^{213}$ indicates the transposition of the first two indices of a third-order tensor, that is, $[H_{inj}]^{213} = H_{nij}$. In component form, equation (2) can be written as

$$H_{ijn}(\mathbf{r},\, t;\, \mathbf{r}_{\mathrm{S}}) \;=\; \frac{1}{2}\left[\partial_i G_{jn}(\mathbf{r},\, t;\, \mathbf{r}_{\mathrm{S}}) \;+\; \partial_j G_{in}(\mathbf{r},\, t;\, \mathbf{r}_{\mathrm{S}})\right]. \qquad (3)$$

This third-order tensor represents the strain associated with the Green's tensors and we call it the strain Green's tensor (SGT). The SGT is symmetric with respect to its first and second indices and therefore it has only 18 independent elements. In seismology, many expressions involve the spatial gradient of the Green's tensor instead of the Green's tensor itself; as a result, the SGT defined in equations (2) and (3) is a more immediately used quantity, and making it available can often improve the efficiency in numerical calculations. For example, the displacement field from a point double-couple earthquake source can be expressed as (e.g., Aki and Richards, 2000, equation 3.23):

$$u_n(\mathbf{r},\, t;\, \mathbf{r}_{\mathrm{S}}) \;=\; \partial_i^{\mathrm{S}} G_{nj}(\mathbf{r},\, t;\, \mathbf{r}_{\mathrm{S}}) M_{ji}, \qquad (4)$$

where $\mathbf{M}$ is the moment tensor and the superscript S to the gradient operator indicates that it acts on the source coordinates. Taking the symmetry of the moment tensor into account and applying the reciprocity of the Green's tensor, equation (4) can be written as:

$$u_n(\mathbf{r},\, t;\, \mathbf{r}_{\mathrm{S}}) \;=\; \frac{1}{2}\left[\partial_i^{\mathrm{S}} G_{jn}(\mathbf{r}_{\mathrm{S}},\, t;\, \mathbf{r}) \;+\; \partial_j^{\mathrm{S}} G_{in}(\mathbf{r}_{\mathrm{S}},\, t;\, \mathbf{r})\right] M_{ji}. \qquad (5)$$

Thus we have

$$u_n(\mathbf{r},\, t;\, \mathbf{r}_{\mathrm{S}}) \;=\; H_{ijn}(\mathbf{r}_{\mathrm{S}},\, t;\, \mathbf{r}) M_{ji} \quad \text{or} \quad \mathbf{u}(\mathbf{r},\, t;\, \mathbf{r}_{\mathrm{S}}) \;=\; \mathbf{M}{:}\mathbf{H}(\mathbf{r}_{\mathrm{S}},\, t;\, \mathbf{r}). \qquad (6)$$

Equation (6) provides an immediate linear relationship between the displacement and the moment tensor. Therefore, the elements of the SGT can be used in earthquake source-parameter inversions to obtain the partial derivatives of the seismic data with respect to the moment tensor elements.

Because the SGT is immediately linked to the earthquake-generated displacement field, the capability of efficiently providing the SGT can greatly improve the efficiency in the modeling of seismic data. Most of the seismic algorithms currently in use, such as the normal-mode summation, finite-difference, finite-element, and spectral-element methods, only provide the solutions to the wave equation, that is, the displacement field. A simple solution for obtaining the SGTs is to use those algorithms to compute the Green's tensor and then obtain the SGTs by taking numerical differentiations with respect to the spatial coordinates. For a given location $\mathbf{r}$, a single finite-difference simulation with a unit impulsive force acting at $\mathbf{r}$ in $\hat{\mathbf{e}}_n$ direction provides the three Green's tensor elements $G_{in}(\mathbf{r}', t; \mathbf{r})$ ($i = 1, 2, 3$) at all the grid points $\mathbf{r}'$, and the full nine-element Green's tensor (for the given location $\mathbf{r}$) can be obtained by three simulations with the unit impulsive forces in three orthogonal directions $n = 1$, 2, and 3. Then, the strain Green's tensor elements in equation (5), $[\partial_i^{\mathrm{S}} G_{jn}(\mathbf{r}_{\mathrm{S}}, t; \mathbf{r}) + \partial_j^{\mathrm{S}} G_{in}(\mathbf{r}_{\mathrm{S}}, t; \mathbf{r})]$, are calculated by numerically differentiating the Green's tensor elements $G_{in}(\mathbf{r}', t; \mathbf{r})$ at $\mathbf{r}' = \mathbf{r}_{\mathrm{S}}$. As a result, the accuracy of such an approach depends on the grid size used in numerical differentiation and this in turn affects the efficiency of the numerical scheme.

There are different approaches to avoid taking numerical differentiation in computing the SGTs efficiently and without the loss of accuracy. The approach applicable to normal-mode summation involves the horizontal derivatives of the surface spherical harmonics and radial derivatives of the radial eigenfunctions and will be dealt with in a separate publication. In this article, we focus on the approaches that apply to numerical algorithms such as finite-difference, finite-element, and spectral-element methods. A common feature in these algorithms is that they all explicitly use the spatial gradients of displacement (or velocity) and the stress (or stress rate) in their calculations. Therefore, for a given location $\mathbf{r}$, we can run the simulations for the three orthogonal forces and output the relevant elements to directly obtain the SGTs $[\partial_i^{r'} G_{jn}(\mathbf{r}', t; \mathbf{r}) + \partial_j^{r'} G_{in}(\mathbf{r}', t; \mathbf{r})]/2$ or H_{ijn}

($\mathbf{r}'$, t; $\mathbf{r}$) without going through the Green's tensor G_{in} ($\mathbf{r}'$, t; $\mathbf{r}$) and the numerical differentiations, thus improving both the efficiency and accuracy of the algorithm.

Efficient 3D Synthetic Calculations by Reciprocity

In seismic structure and source studies, forward modeling of seismic-wave propagation is a universal requirement. This often presents a particular challenge when the seismic structure in use is complex and purely numerical methods such as finite-difference, finite-element, and spectral-element methods must be used. In the conventional approach, we usually use the known location of an earthquake source and its focal mechanism as inputs and one numerical simulation will give us the three-component displacement field at all the grid points generated by the earthquake. This is the proper approach if the purpose is to obtain the synthetic seismograms at many stations from a handful of earthquakes, because the number of numerical simulations is simply the number of earthquake sources. If the number of sources involved is too large, however, the CPU time required to run the equally large number of numerical simulations can be prohibitive. An alternative approach that is much more efficient when the sources greatly outnumber the stations is to use the source-receiver reciprocity so that the number of simulations is proportional to the number of stations (e.g., Bouchon, 1976; Graves and Clayton, 1992; Graves and Wald, 2001; Eisner and Clayton, 2001). Eisner and Clayton (2001) proposed to compute the Green's tensors from the receivers by the finite-difference method and then obtain the gradients of the Green's tensors at the earthquake source locations by numerical differentiation. Here we make a small modification to the previous studies by adopting the strain Green's tensor that is already available in the finite-difference process and is also more immediately linked to the displacement field than the Green's tensor. With a few lines of change to the finite-difference code, we can output the SGTs instead of the displacements. In our implementation, to obtain the complete SGT for a given receiver we need three finite-difference simulations because we need the strain fields from all three orthogonal-unit-impulsive point forces acting at the receiver. By saving the 18 independent elements of the SGTs, we not only are guaranteed to achieve the same accuracy in the synthetics as the forward finite-difference simulations, but also reduce the CPU time spent on the numerical differentiations. Figure 1 shows the three-component synthetic seismograms at a Southern California Seismic Network (SCSN) station USC (see Fig. 2 for the station location) computed by a conventional forward finite-difference simulation from a source in Yorba Linda and by reciprocity (equation 6) by using the strain Green's tensor for the station USC. For validation purposes we used a two-layer model in this example and we also computed the synthetics using the frequency-wavenumber approach (Zhu and Rivera, 2002). We see that an excellent agreement exists among the results from the three different approaches. In particular, the dashed

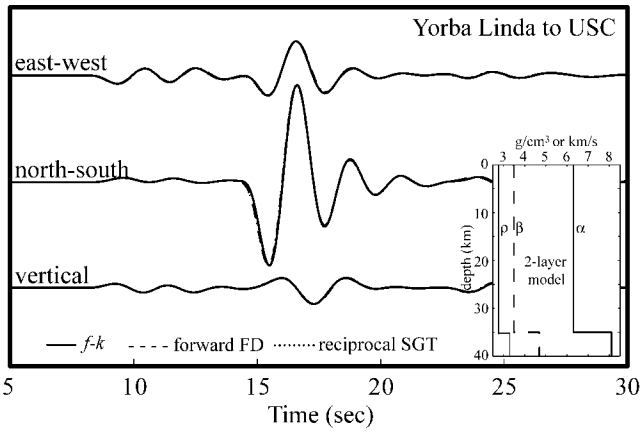

Figure 1. Comparison of synthetic seismograms from the Yorba Linda earthquake to station USC. The three-component synthetics are computed in the two-layer model by three different methods: the frequency-wavenumber integration method (solid line), the forward finite-difference simulation (dashed line), and the strain Green's tensor from station USC.

(forward finite-difference) and the dotted (strain Green's tensor) lines match each other almost exactly.

In realistic 3D structural models, the SGT approach also enables us to compute synthetic seismograms with the same accuracy as the forward finite-difference simulations. Figure 3 shows a comparison of the forward and reciprocal synthetics using the 3D velocity model SCEC CVM 3.0 developed by the Southern California Earthquake Center (Magistrale *et al.*, 2000; Kohler *et al.*, 2003). The waveforms from the two different approaches match each other completely.

In calculating the SGTs for seismic stations, the free-surface boundary condition must be carefully observed because we need to put the orthogonal forces at the station locations that are mostly on the free surface. In most 3D staggered-grid finite-difference algorithms (e.g., Olsen, 1994; Graves, 1996), a velocity-stress formulation is used and the sources are implemented in terms of contributions to either the velocities by body forces or the stresses by double couples. In the staggered-grid algorithm, the horizontal velocities are defined at grid points right on the zero-stress free surface, yet the vertical velocity is defined at grid points one-half grid size from the free surface. As a result, the SGT elements from the two horizontal forces are accurate, whereas the elements from the vertical force are off by exactly a factor of 2, that is, a vertical force with an amplitude of two units must be used to obtain accurate SGT elements. The excellent agreement of the vertical-component synthetics in Figures 1 and 3 proves that this is the case. Eisner and Clayton (2001) observed that the vertical force should be located one-half grid size below the free surface to achieve accurate Green's tensor results.

With the numerical accuracy established, the best way to harness the power of the strain Green's tensor approach is to build a database of the SGTs for the available seismic

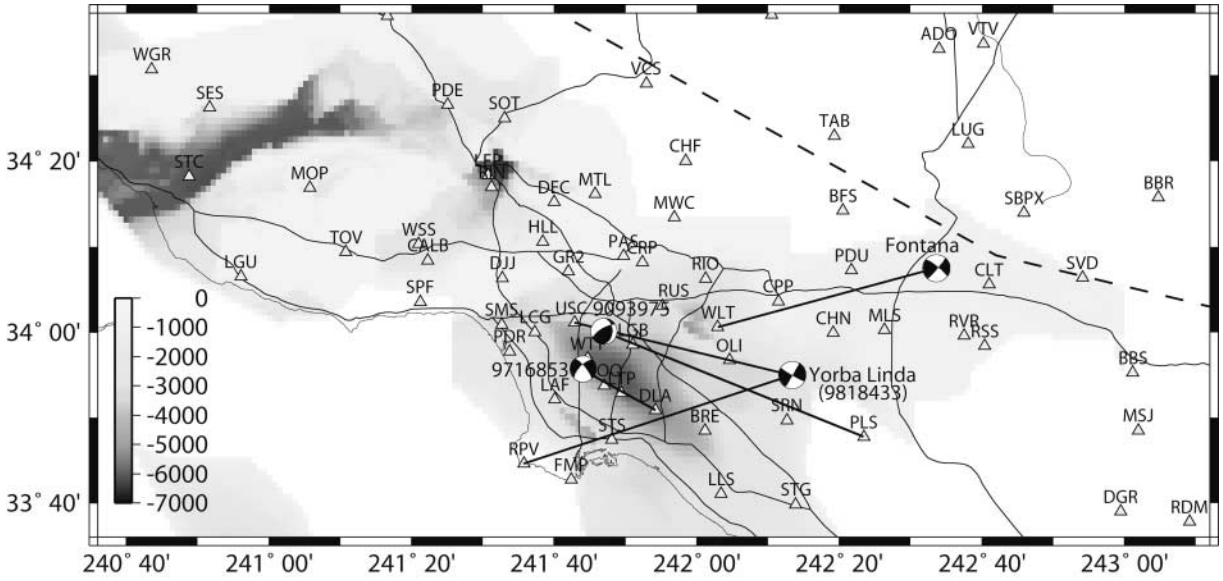

Figure 2. Map of the Los Angeles Basin area used in establishing the SGT database. The gray scale indicates the depth of the sedimentary basins in meters. The beach balls show the locations and focal mechanisms of earthquakes. Triangles are the locations of the SCSN stations. Dashed line shows the San Andreas fault.

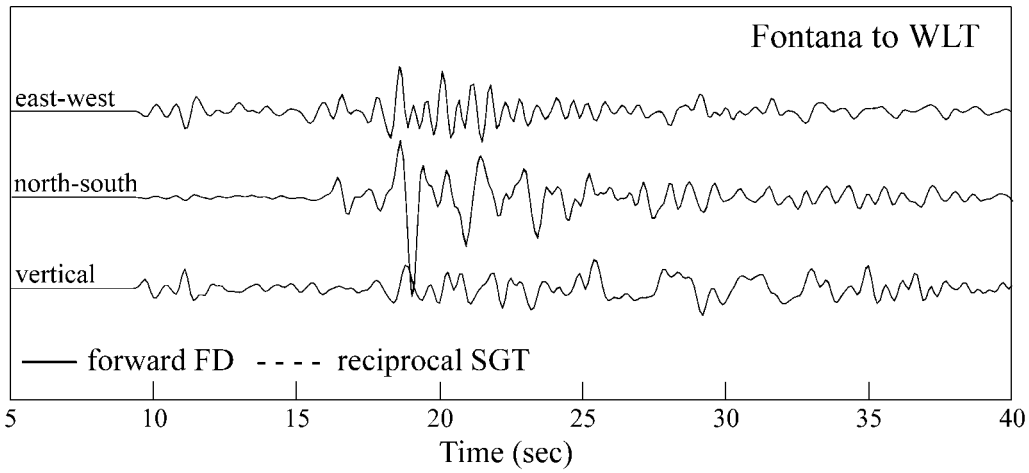

Figure 3. Comparison of synthetic seismograms from the Fontana earthquake to station WLT (see Fig. 2 for the source-station path) calculated by forward finite-difference simulation (solid line) and by reciprocity using strain Green's tensor from WLT. There are dashed lines. They are hidden under the solid lines because of the excellent agreement between the seismograms obtained by the two different methods. The structural model used is the 3D model SCEC CVM 3.0.

stations so that all subsequent waveform-based modeling required by source and structure inversions are reduced to simple calculations using the SGT elements extracted from the database rather than running full numerical simulations each time new earthquakes are added. We have established the SGT database for the 64 SCSN stations in the region shown in Figure 2. For a given station at $\mathbf{r}_R$, we ran three finite-difference simulations for the three orthogonal-unit-impulsive forces at $\mathbf{r}_R$ to obtain the strain Green's tensor $\mathbf{H}(\mathbf{r}', t; \mathbf{r}_R)$ at all the grid points $\mathbf{r}'$. The numerical result formed a dataset on a 4D volume $(\mathbf{r}', t) \in R^4$ and was stored on a disk. This process was repeated for all stations on the same 4D volume to establish the 64-station SGT database. The regional 3D reference model SCEC CVM 3.0 was used for this database. The 4D volume involves the spatial region shown in Figure 2 down to a depth of 30 km and 60 sec in time. A spatial grid spacing of 200 m and a timestep of 0.01 sec were used in the finite-difference simulations to achieve accurate simulation results up to 1 Hz. It took about 1 hr to run each simulation, or a total of about one week for all 64

stations, using 128 processors on the Linux cluster at the University of Southern California. The entire 64-station SGT database occupies about 5 TB of disk space at a sampling rate of 600 m in space and 0.1 sec in time. The SGT applications to source and structure studies discussed in the next two sections are based on this database.

Earthquake Source Inversions

In earthquake-prone areas such as Southern California, accurate representations of earthquake sources are important both for reliable seismic-hazard analysis and for realistic interpretation of regional geological and tectonic structures. Currently, focal mechanisms of earthquakes in Southern California are routinely determined from SCSN first-motion data for earthquakes as small as $M_L \sim 2.0$–2.5 (Hauksson, 2000), and complete Centroid Moment Tensor (CMT) (Harvard Seismology, 2006) solutions can be recovered from waveforms for M_L greater than 3.0–3.5 (Zhu and Helmberger, 1996; Pasyanos *et al.*, 1996; Liu *et al.*, 2004). In the waveform inversion approach, a certain measure of the waveform anomaly in either the time or the frequency domain is minimized by an optimization method. To reduce computational cost, the Green's functions are usually computed in simple 1D structural models, which are often inadequate for areas with complex 3D seismic structures. To account for 3D structural heterogeneities, Liu *et al.* (2004) developed a waveform inversion technique using 3D Green's functions and Fréchet derivatives computed in a 3D velocity model (Hauksson, 2000; Zhu and Kanamori, 2000; Süss and Shaw, 2003) by spectral-element method. That approach, however, is computationally demanding and therefore is not suitable for fast determination of earthquake source parameters.

Following Chen *et al.* (2005), we quantify the waveform perturbation caused by possible errors in the focal mechanism in the following way:

$$u_n(\mathbf{r}_R, \omega) = u_n^0(\mathbf{r}_R, \omega)\exp[i\omega\delta t_p(\omega) - \omega\delta t_q(\omega)], \quad (7)$$

where $u_n^0(\mathbf{r}_R, \omega)$ is the waveform for the starting source model. The waveform anomalies are represented by the frequency-dependent arrival-time anomaly $\delta t_p(\omega)$ and amplitude-reduction time $\delta t_q(\omega)$. These parameters were the so-called generalized seismological data functionals (GSDFs) introduced by Gee and Jordan (1992). They have been used in global and regional structure and source studies using long-period (up to 20 sec) records (Gaherty *et al.*, 1996; Katzman *et al.*, 1998; McGuire *et al.*, 2001). Chen (2005) implemented this approach to small-scale regional and local structure and source studies using short-period (10 sec to 5 Hz) records and developed an efficient and semi-automated procedure to measure $\delta t_p(\omega)$ and $\delta t_q(\omega)$ (Chen 2005; Chen *et al.*, 2005; P. Chen, T. H. Jordan, and L. Zhao, unpublished manuscript, 2006). According to Kikuchi and Kanamori (1991), we can decompose a general moment tensor **M** into six elementary basis functions. The displacement field due to a general moment tensor can thus be expressed as a linear combination of the displacements for the six moment basis functions:

$$u_n(\mathbf{r}_R, t) = \sum_{m=1}^{6} a_m g_{nm}(t). \quad (8)$$

Here, $g_{nm}(t)$, the n-component displacement for basis moment tensor m, is computed from the SGT at the source location by reciprocity. The coefficients a_m are related to the moment tensor elements and are to be determined. Therefore, with the measurements of $\delta t_p(\omega)$ and $\delta t_q(\omega)$ at several discrete frequencies ω_i, we can invert for the perturbations of a_m using the following partial derivatives:

$$\delta t_q(\omega_i) = -\sum_{m=1}^{6} \frac{\mathrm{Re}[u_n^0(\omega_i)] \cdot \mathrm{Re}[g_{nm}(\omega_i)] + \mathrm{Im}[u_n^0(\omega_i)] \cdot \mathrm{Im}[g_{nm}(\omega_i)]}{\omega_i |u_n^0(\omega_i)|^2} \delta a_m, \quad (9)$$

$$\delta t_p(\omega_i) = \sum_{m=1}^{6} \frac{\mathrm{Re}[u_n^0(\omega_i)] \cdot \mathrm{Im}[g_{nm}(\omega_i)] - \mathrm{Im}[u_n^0(\omega_i)] \cdot \mathrm{Re}[g_{nm}(\omega_i)]}{\omega_i |u_n^0(\omega_i)|^2} \delta a_m. \quad (10)$$

The perturbations δa_m can then be used to update the source model. Here, $u_n(\omega_i)$ and $g_{nm}(\omega_i)$ are the Fourier transforms of $u_n^0(t)$ and $g_{nm}(t)$ at the measuring frequency ω_i, respectively. The strain Green's tensor approach leads to efficient calculations of partial derivatives in equations (9) and (10), which enables us to use 3D waveforms to iteratively invert and update the source models.

The example in Figure 4 demonstrates the effectiveness of this approach. The focal mechanism shown by the beach ball at the bottom was assumed to be the "truth." We chose 39 SCSN stations and computed their three-component waveforms based on this "true focal mechanism" using our SGT database. These waveforms were taken as "records" in our automated optimization procedure. The beach ball at the top in Figure 4 shows the initial solution for the focal mechanism. The SGT-generated synthetics for the initial solution and the "recorded" waveforms were used to measure the frequency-dependent delay times and amplitude-reduction times. All synthetic and recorded waveforms were 60-sec-long time series, and the measurements were made on the entire waveforms bandpass filtered by a fourth-order Butterworth filter with corner frequencies of 0.001 Hz and 0.3 Hz. The δt_p and δt_q measurements were obtained at 10 discrete frequencies between 0.1 Hz and 0.3 Hz, and the perturbations δa_m were inverted using equations (9) and (10). In our experiments, we have found that between delay times and amplitude-reduction times, the latter are more robust in

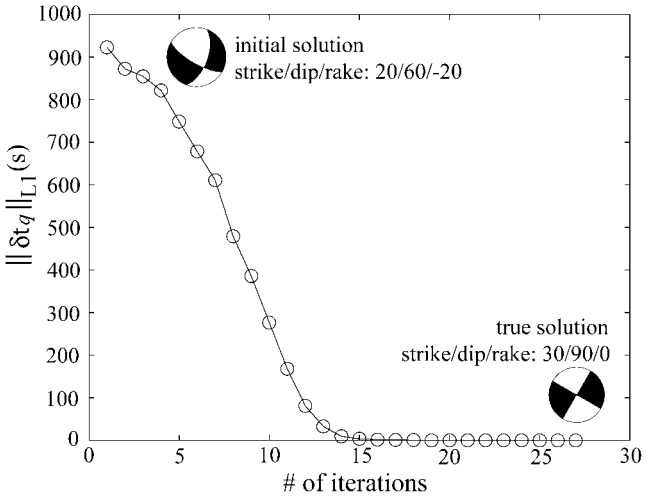

Figure 4. A demonstration of the iterative process in the CMT inversion. The fault-plane solution at the bottom is used to generate the recorded seismogram, whereas the fault-plane solution at the top and after each iteration provide the synthetic seismograms. The true solution is reached after 15 iterations.

source-parameter inversions. This is expected because the moment tensor, which determines the source-radiation pattern, affects the amplitudes of the individual arrivals more than their arrival times. We then update the focal mechanism, which was used as a new initial solution for the next iteration. Figure 4 shows that the true solution was reached after 15 iterations. The efficiency in this approach can only be achieved through the use of the SGT database. When the focal mechanism is updated after each iteration, the synthetic seismograms can be calculated very quickly using the SGT database without the need for finite-difference simulations using the new focal mechanism.

We have applied our method to the recovery of source mechanisms of small to moderate earthquakes around the Los Angeles Basin area. We collected a total of 27 events for which broadband records with good signal-to-noise ratios are available from at least five stations in our studied region (Fig. 1). To initiate the iterative optimization processes, we took the origin times and hypocenters from the Shearer, Hauksson, Lin, and Kilb (SHLK) catalog (Shearer *et al.*, 2005). In the SHLK catalog, the events have been carefully relocated; therefore, in our source-parameter inversions we do not perturb the hypocenter locations. For the starting source models, we estimated the focal mechanisms from first-motion data using the HASH algorithm by Hardebeck and Shearer (2002) to carry out the grid search for suitable dip, rake, and strike angles that best fit the polarities of the first motions. The 3D synthetic seismograms were all computed using the SGT database. Both the observed and synthetic seismograms were 60 sec long and were bandpass filtered between 0.001 Hz and 0.3 Hz using a fourth-order Butterworth filter, and the amplitude-reduction times δt_q were measured automatically at 10 discrete frequencies between 0.1 Hz and 0.3 Hz using the entire waveforms. In all the iterative inversions, the solutions converge after 10 $\sim$ 20 iterations.

Figure 5 shows the comparison of our solutions for the 27 local earthquakes with Hauksson's focal mechanisms determined from first-motion data. For most of the earthquakes, the two solutions are in good agreement. The detailed solutions of the 27 events are given in Table 1. The overall variance reduction in δt_q with respect to Hauksson's solutions is $\sim$14%, suggesting that our fault-plane solutions lead to improvements in waveform fit between synthetic and recorded seismograms (Gee and Jordan, 1992; Chen *et al.*, 2005). Hauksson's focal-mechanism solutions were determined by the first-motion data from unrelocated events in a 1D structure and are therefore subject to errors in earthquake locations and 3D structure larger than our results, which are obtained by inverting waveforms from relocated events in 3D structure.

The efficiency afforded by the SGT database coupled with the automated waveform-based measurement process permits us to conduct extensive search of the solution space to effectively avoid being trapped into a local minimum. The average time for determining a CMT solution is about 5 min on a single Pentium III computer. Thus the SGT approach provides a practical means to obtain reliable and near-real-time moment tensor solutions in 3D structural models through the nonlinear inversion of frequency-dependent amplitude anomalies.

Efficient Fréchet Kernel Calculations for Structural Inversions

The SGT approach can also be applied to the calculations of the sensitivity or Fréchet kernels that are used in structural inversions and provides an even more drastic improvement in numerical efficiency. Starting from the pioneering work of Li and Tanimoto (1993), more physically realistic sensitivity kernels have been introduced into global and regional structural studies using 1D (depth-dependent) reference models. Dahlen *et al.* (2000) and Hung *et al.* (2000) presented an efficient algorithm for computing the banana-doughnut kernels for body waves by using geometrical ray theory, Zhou *et al.* (2004) adopted surface-wave method to model surface-wave phase delays, whereas Zhao *et al.* (2000) and Zhao and Jordan (2006) took the normal-mode approach to obtain accurate Fréchet kernels for any arbitrary arrivals. In studying small-scale subsurface structures, however, complex 3D reference models are necessary, and algorithms have been developed to compute the sensitivity kernels based on purely numerical methods such as the finite-difference method (Zhao *et al.*, 2005) and the spectral-element method (Liu and Tromp, unpublished manuscript, 2006).

Similar to source-parameter inversions, in structural studies we related the delay times and amplitude-reduction times to our target of interest: the perturbations of the earth's structural parameters. Every datum δd obtained on a record from a specific source-receiver pair can be expressed in

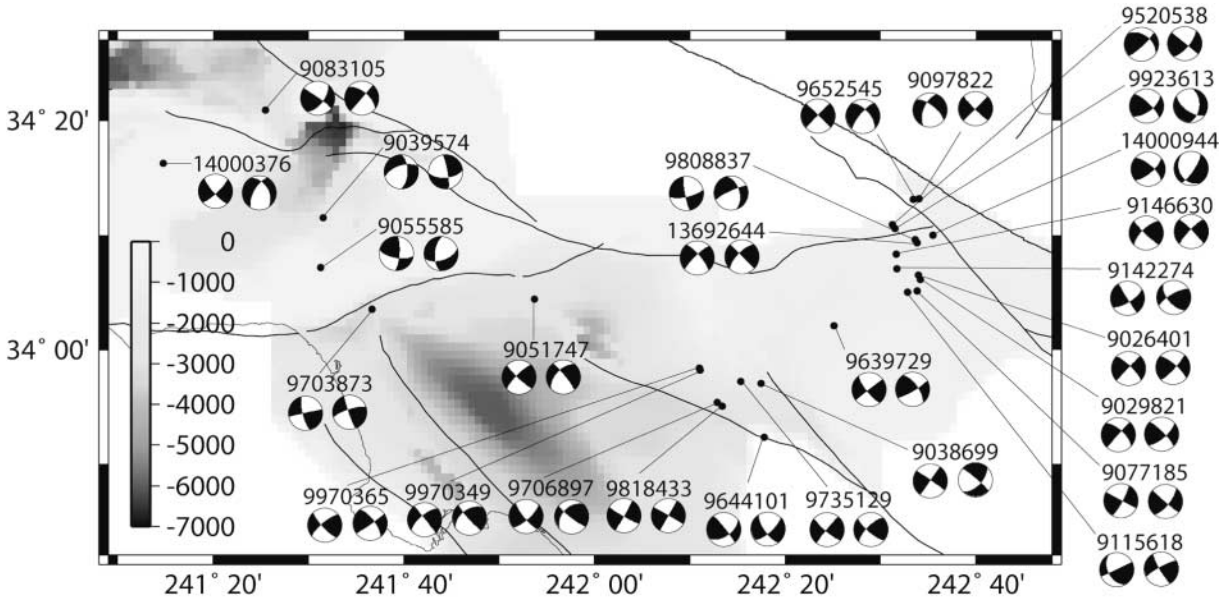

Figure 5. Comparison of the fault-plane solutions we determined with those from Southern California Earthquake Data Center. Table 1 lists the source parameters of the 27 local earthquakes in the Los Angeles Basin area. In each pair of the beach balls, the left one shows our result. Major faults in the area are shown by the solid curves. Gray scale indicates the basin depth in meters.

Table 1
Focal Mechanisms for the 27 Events We Have Processed

Cuspid	Lat.	Long.	Depth	Mag.	strl	dip1	rak1	str2	dip2	rak2	Ntra.	$\Delta\sigma$ (%)
14000944	34.1672	−117.408	11.72	3.27	311	69	157	150	30	−150	120	13.3
14000376	34.2722	−118.753	13.81	3.59	139	78	−168	210	65	−50	117	27.4
13692644	34.1562	−117.436	9.251	3.74	319	76	−170	225	70	0	120	2.5
9703873	34.0585	−118.384	8.016	4.24	257	89	14	165	60	180	120	18.4
9051747	34.0740	−118.105	8.247	3.79	225	78	7	225	55	−10	30	16.3
9039574	34.1849	−118.461	11.15	3.35	0	60	−146	85	60	10	24	15.3
9038699	33.9425	−117.713	12.69	4.29	305	87	−180	310	85	150	27	−2.0
9029821	34.1024	−117.430	7.62	3.57	222	89	−24	315	80	160	24	−5.4
9026401	34.1086	−117.434	4.38	3.87	314	78	−178	310	75	170	27	11.8
9083105	34.3497	−118.575	4.241	3.59	37	61	3	40	90	30	45	22.6
9077185	34.0855	−117.436	4.558	3.59	28	80	0	130	85	−160	42	10.5
9055585	34.1200	−118.478	9.309	3.02	100	67	16	185	60	−140	36	1.2
9146630	34.1390	−117.472	13.33	3.53	225	69	7	315	85	−170	81	10.7
9142274	34.1184	−117.471	15.52	3.03	57	70	−3	140	60	160	75	−4.7
9115618	34.0840	−117.452	4.591	3.06	154	45	−180	150	80	170	41	8.7
9097822	34.2206	−117.432	14.94	3.02	204	59	−26	135	85	180	51	24.8
9735129	33.9533	−117.744	12.28	3.97	220	88	10	130	75	160	123	18.1
9706897	33.9227	−117.785	9.26	3.1	141	78	−163	225	45	10	120	6.2
9652545	34.2199	−117.442	9.89	3.84	224	87	−1	220	75	−30	111	−2.8
9644101	33.8724	−117.703	1.86	3.64	321	85	144	145	75	−160	117	17.6
9639729	34.0349	−117.581	9.91	3.35	142	76	−180	325	65	170	117	10.2
9520538	34.1828	−117.479	3.28	3.14	307	46	166	130	90	−160	114	15.9
9970365	33.9733	−117.816	16.33	3.18	137	77	166	55	85	20	111	10.6
9970349	33.9705	−117.815	16.74	3.53	321	88	−159	235	50	10	114	14.1
9923613	34.1773	−117.474	4.0	3.38	52	62	17	125	60	−130	117	14.1
9818433	33.9180	−117.781	9.47	4.75	120	86	−178	30	90	20	117	28.4
9808837	34.1604	−117.439	8.96	3.04	77	72	−9	245	80	−40	120	23.6

Column 1, the event id in the SCSN catalog; columns 2–5, latitudes (Lat.), longitudes (Long.), depths, and magnitudes (Mag.) of the events. Columns 6–8, the strike, dip, and rake angles of the focal mechanisms we determined using the 3D velocity model are listed; Columns 9–11, Hauksson's focal mechanisms are listed. The last two columns are the number of seismograms used and the variance reduction from Hauksson's solutions.

terms of the perturbation of a model parameter δc through a linear integral over the volume of the earth model:

$$\delta d(\mathbf{r}_R;\ \mathbf{r}_S) = \int_{\oplus} K_c^d(\mathbf{r}_R;\ \mathbf{r};\ \mathbf{r}_S)\delta c(\mathbf{r})d^3\mathbf{r}, \qquad (11)$$

where K_c^d ($\mathbf{r}_R$; $\mathbf{r}$; $\mathbf{r}_S$), referred to as the Fréchet kernel, represents the degree to which the observed anomaly δd depends on the local model perturbation $\delta c(\mathbf{r})$. Thus K_c^d ($\mathbf{r}_R$; $\mathbf{r}$; $\mathbf{r}_S$) is also often called the sensitivity kernel. If a sufficient collection of the data and their Fréchet kernels are available, then equation (11) will provide a system of linear equations that can be used to invert for the model perturbation.

Because every datum δd measures the difference between recorded and synthetic waveforms, it can always be expressed in terms of the synthetic waveform $\mathbf{u}(\mathbf{r}_R;\ \mathbf{r}_S)$ in the reference model and its perturbation $\delta\mathbf{u}(\mathbf{r}_R;\ \mathbf{r}_S)$. For example, the travel-time anomaly can be expressed in terms of the time-domain wave-fields as (Dahlen *et al.*, 2000; Zhao *et al.*, 2000):

$$\delta\tau_p(\mathbf{r}_R;\ \mathbf{r}_S) = \int_{-\infty}^{\infty} \dot{u}(\mathbf{r}_R,\ t;\ \mathbf{r}_S)\delta u(\mathbf{r}_R,\ t;\ \mathbf{r}_S)dt \Big/ \int_{-\infty}^{\infty} \ddot{u}(\mathbf{r}_R,\ t;\ \mathbf{r}_S)\, u(\mathbf{r}_R,\ t;\ \mathbf{r}_S)dt, \qquad (12)$$

where $\dot{\mathbf{u}}$ and $\ddot{\mathbf{u}}$ are the first- and second-time derivatives of $\mathbf{u}$, respectively. Similar expressions in terms of $\mathbf{u}$ and $\delta\mathbf{u}$ can be derived for any waveform-derived measurements. The travel-time anomaly $\delta\tau_p$ in equation (12) is defined such that a positive value indicates a delay of the recorded waveform relative to the synthetic. Thus, we call it the delay time. The waveform perturbation $\delta\mathbf{u}$ due to a small perturbation in the elasticity tensor can be expressed as (Zhao *et al.*, 2005):

$$\delta\mathbf{u}(\mathbf{r}_R,\ t;\ \mathbf{r}_S) = \int_{\oplus}\int_{-\infty}^{\infty} [\nabla\mathbf{G}(\mathbf{r}_R,\ t\ -\ \tau;\ \mathbf{r})]^{213} : \delta\mathbf{C}(\mathbf{r}) : (\nabla\mathbf{u}(\mathbf{r},\ \tau;\ \mathbf{r}_S)]d\tau d^3\mathbf{r}, \qquad (13)$$

where $\delta\mathbf{C}(\mathbf{r})$ is the perturbation of the fourth-order elasticity tensor and the integral is over the earth volume of interest. For the perturbation of any specific structural parameter such as the *P*-wave speed α, the expression for its delay-time Fréchet kernel $K_c^{\tau_p}$ ($\mathbf{r}_R$; $\mathbf{r}$; $\mathbf{r}_S$) can be derived by substituting equation (13) into equation (12), retaining the elements in $\delta\mathbf{C}(\mathbf{r})$ that contribute to α and identifying the kernel for the spatial integral.

The most important and intractable quantity in computing the Fréchet kernels is the waveform perturbation expressed in equation (13). To evaluate this expression at any given point $\mathbf{r}$ in the model, we need the spatial gradients of two wavefields (see Fig. 6): the displacement $\mathbf{u}(\mathbf{r};\ \mathbf{r}_S)$ from the source to $\mathbf{r}$ and the Green's tensor $\mathbf{G}(\mathbf{r}_R;\ \mathbf{r})$ from $\mathbf{r}$ to the receiver. The symmetry property of the elasticity tensor:

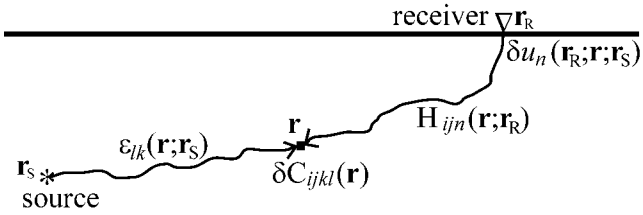

Figure 6. Schematic diagram illustrating the geometry of the wave-field quantities in equation (19) involved in the calculation of the contribution to the perturbation of the displacement at the receiver by a model perturbation at $\mathbf{r}$.

$$\delta C_{ijkl} = \delta C_{ijlk}, \qquad (14)$$

allows us to recast equation (13) as:

$$\delta\mathbf{u}(\mathbf{r}_R,\ t;\ \mathbf{r}_S) = \int_{\oplus}\int_{-\infty}^{\infty} [\nabla\mathbf{G}(\mathbf{r}_R,\ t\ -\ \tau;\ \mathbf{r})]^{213} : \delta\mathbf{C}(\mathbf{r}) : [\boldsymbol{\varepsilon}(\mathbf{r},\ \tau;\ \mathbf{r}_S)]d\tau d^3\mathbf{r}, \qquad (15)$$

or in the frequency domain

$$\delta\mathbf{u}(\mathbf{r}_R,\ \omega;\ \mathbf{r}_S) = \int_{\oplus} [\nabla\mathbf{G}(\mathbf{r}_R,\ \omega;\ \mathbf{r})]^{213} : \delta\mathbf{C}(\mathbf{r}) : [\boldsymbol{\varepsilon}(\mathbf{r},\ \omega;\ \mathbf{r}_S)]d^3\mathbf{r}, \qquad (16)$$

where the strain tensor $\boldsymbol{\varepsilon}$ is defined in equation (1). In an algorithm purely based on numerical methods such as finite difference, the strain tensor at every point in the model can be obtained by a single numerical simulation from the earthquake source location $\mathbf{r}_S$. However, the spatial gradient of the Green's tensor $\nabla\mathbf{G}(\mathbf{r}_R,\ t\ -\ \tau;\ \mathbf{r})$ would be impossible to calculate because it calls for numerical simulations from all the points in the model to the receiver location $\mathbf{r}_R$. The reciprocity property and the SGTs provide the perfect rescue that makes the evaluation of waveform perturbations tractable. Taking the advantage of another symmetry properties of the elasticity tensor:

$$\delta C_{ijkl} = \delta C_{jikl}, \qquad (17)$$

equation (15) can be written as:

$$\delta\mathbf{u}(\mathbf{r}_R,\ t;\ \mathbf{r}_S) = \int_{\oplus}\int_{-\infty}^{\infty} [\delta C(\mathbf{r}) : \boldsymbol{\varepsilon}(\mathbf{r},\ \tau;\ \mathbf{r}_S)] : \mathbf{H}(\mathbf{r},\ t\ -\ \tau;\ \mathbf{r}_R)d\tau d^3\mathbf{r}, \qquad (18)$$

or

$$\delta\mathbf{u}_n(\mathbf{r}_R,\ t;\ \mathbf{r}_S) = \int_{\oplus}\int_{-\infty}^{\infty} H_{ijn}(\mathbf{r},\ t\ -\ \tau;\ \mathbf{r}_R)\ \delta C_{ijkl}(\mathbf{r})\ \varepsilon_{lk}(\mathbf{r},\ \tau;\ \mathbf{r}_S)d\tau d^3\mathbf{r}. \qquad (19)$$

Thus, instead of the using $\nabla\mathbf{G}(\mathbf{r}_R, t - \tau; \mathbf{r})$, which requires the same number of numerical simulations as the number of points in the model, we can use $\mathbf{H}(\mathbf{r}, t - \tau; \mathbf{r}_R)$, the SGT from the receiver that requires only three numerical simulations for the three orthogonal single forces acting at the receiver. This result provides a means to improve the efficiency in the algorithm for calculating the Fréchet kernels used in seismic tomography inversions.

Numerical results of the delay-time Fréchet kernels have been presented in Zhao *et al.* (2005) for a variety of local phases. In that article, the Green's tensor $\mathbf{G}(\mathbf{r}, t; \mathbf{r}_R)$ and the wave field $\mathbf{u}(\mathbf{r}, t; \mathbf{r}_S)$ were computed by finite-difference simulations. They were transformed by fast Fourier transform (FFT) into the frequency domain and substituted into the integrand in equation (16) to obtain the frequency-domain waveform perturbation due to the perturbation of a given model parameter $\delta C_{ijkl}(\mathbf{r})$ at $\mathbf{r}$. This waveform perturbation was then transformed back to the time domain by an inverse FFT and used in equation (12) to calculate the corresponding delay-time perturbation, which is essentially the delay-time Fréchet kernel for the model parameter $\delta C_{ijkl}(\mathbf{r})$ at $\mathbf{r}$. Zhao *et al.* (2005) pointed out that numerical noises appear in the Fréchet kernels because of (1) numerical dispersion in the finite-difference method, (2) the inaccuracies in the free-surface and absorption-boundary conditions, and (3) the forward and inverse FFTs in the evaluation of $\delta\mathbf{u}(\mathbf{r}_R, \omega; \mathbf{r}_S)$ and $\delta\mathbf{u}(\mathbf{r}_R, t; \mathbf{r}_S)$. Because the finite-difference simulations were limited in both frequency band (up to 1 Hz) and time span (60 sec), the FFT-dependent algorithm inevitably introduces some numerical noises in the resulting kernels. These numerical noises are especially obvious in the *P*-wave kernels near the surface as they appear to be noncausal, as seen in figure 10 of Zhao *et al.* (2005) and in Figure 7 in this article. Here, we have revised the algorithm in two aspects: (1) we obtain the strain Green's tensors $\mathbf{H}(\mathbf{r}, t; \mathbf{r}_R)$ and the strain fields $\boldsymbol{\varepsilon}(\mathbf{r}, t; \mathbf{r}_S)$ directly from finite-difference simulations so that no spatial numerical differentiations are needed; and (2) equation (19) is used to compute the time-domain wave-field perturbation $\delta u(\mathbf{r}_R, t; \mathbf{r}_S)$ directly so that all the calculations are carried out completely in the time domain without the need for FFTs. Figure 7 shows examples of Fréchet kernels for the delay times of three direct *P* waves (see Fig. 2 for the source-station geometries). In Zhao *et al.* (2005), the kernels were computed for the frequency band up to 1 Hz with a dominate period of 1.5 sec (left column in Fig. 7), whereas the kernels calculated using the revised algorithm (right column in Fig. 7) were computed over the frequency band 0.6 ± 0.12 Hz. The lowering of the dominant frequency and the narrowing of the frequency band caused the new set of kernels to have wider distributions of sensitivities. However, the noncausal numerical noises in the kernels obtained by the frequency-domain algorithm have clearly been completely eliminated.

The implementation of the algorithm based on the reciprocity and the SGT database for the Los Angeles area stations (Fig. 2) has enabled us to conduct the most fully 3D tomography inversion ever practiced: inverting for both *P*- and *S*-wave speed perturbations independently using 3D full-wave Fréchet kernels calculated for 3D reference models (Chen *et al.*, 2006). With this approach, it is also feasible to further improve the structural models iteratively to remedy the possible effect of the linearization.

Discussion

We have demonstrated that the reciprocal strain Green's tensors provide an accurate and efficient approach to calculate synthetic seismograms in situations in which the sources greatly outnumber the stations. The accuracy of the seismograms obtained by the SGTs is the same as that of the forward finite-difference simulations even in complex 3D velocity structures. This alternative waveform-synthesizing approach has been adopted by the Southern California Earthquake Center's Community Modeling Environment in its CyberShake project (http://epicenter.usc.edu/cmeportal/CyberShake.html): a fully finite-difference simulation based seismic-hazard analysis in which, for a given site, hundreds of thousands of extended earthquake sources in a complex 3D structural model are required. With the use of reciprocal SGT, only a few finite-difference simulations are needed for each site, and the ground-motion histories from the hundreds of thousands of finite earthquake sources can be calculated very efficiently.

The SGT approach also makes source- and structural-parameter inversions based on 3D reference models feasible. The drastic improvement in numerical efficiency provided by the reciprocity and the SGT database allows us to revise the moment tensor solutions and even the finite moment tensors (Chen *et al.*, 2005) of small earthquakes in 3D structures, which helps in improving the fault-plane solutions and in resolving the fault-plane ambiguity. The reciprocal SGTs are also indispensable in assuring the efficiency in numerical calculations of the sensitivity kernels of waveform-based seismic measurements to *P*- and *S*-wave speed perturbations, thus enabling us to conduct iterative structural inversions to solve the nonlinear regional tomography problems (P. Chen, T. H. Jordan, and L. Zhao, unpublished manuscript, 2006).

Acknowledgments

This research was supported by NSF grant EAR-0308403 and by the Southern California Earthquake Center (SCEC). SCEC is funded by NSF Cooperative Agreement EAR-0106924 and USGS Cooperative Agreement 02HQAG0008. The SCEC contribution number for this article is 981. Numerical computations for the Fréchet kernels described in this article were supported in part by the University of Southern California Center for High Performance Computing and Communications (www.usc.edu/hpcc). Kim B. Olsen's finite-difference code (Olsen 1994) and Lupei Zhu's frequency-wavenumber code (Zhu and Rivera, 2002) were used in some of our numerical calculations. National Science Council of Taiwan is also acknowledged for supporting LZ's visit to the Institute of Earth Sciences, Academia Sinica, where the article was written. Figure 2 was produced by the Generic Mapping Tools of Wessel and Smith (1998).

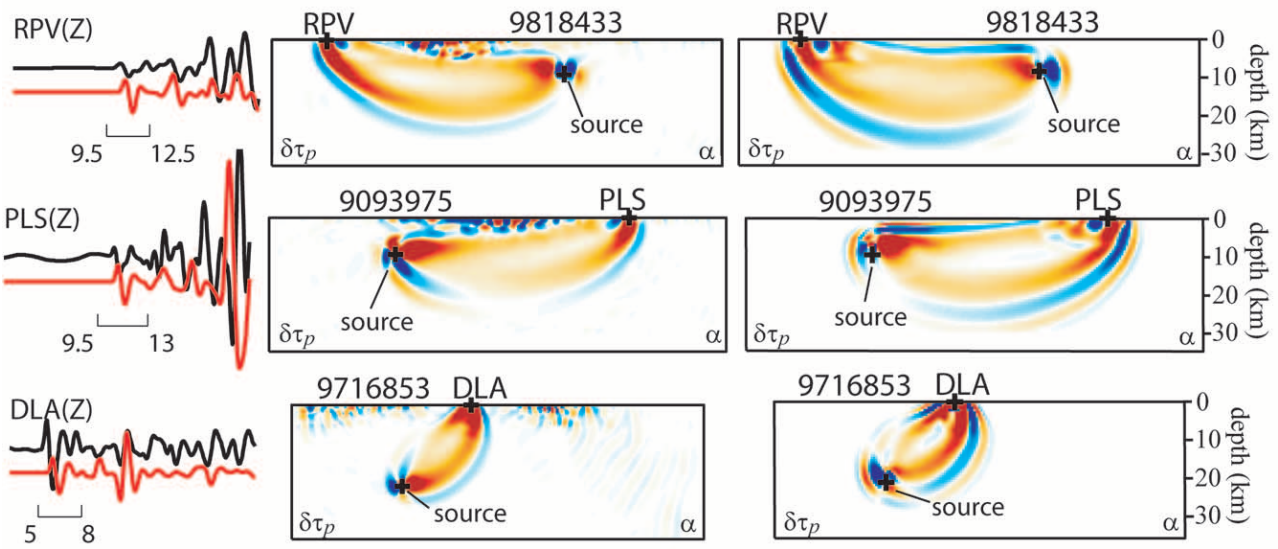

Figure 7. Vertical-component waveforms (first column) and 3D sensitivity (Fréchet) kernels of *P*-wave delay times to the perturbation of *P*-wave speed α. The source and station locations are shown in Figure 2. Recorded waveforms are black, and finite-difference synthetics in SCEC CVM 3.0 are red. The time windows used to obtain the kernels are indicated (in seconds). The kernels in the middle column are those in figure 10 in Zhao *et al.* (2005), whereas the kernels in the right column are kernels for the same phases but computed using the SGTs and a redesigned time-domain-only algorithm. Warm colors indicate negative amplitude, implying that a velocity increase leads to negative delay time or an advance. Noncausal numerical noises can be seen in the kernels in the middle column, especially near the free surface. The noises have been completely eliminated by the new algorithm. The two sets of kernels were computed with different frequency contents, which led to differences in the overall widths of the two sets of kernels.

References

Aki, K., and P. G. Richards (2002). *Quantitative Seismology*, Second Ed., University Science Books, Sausalito, California, 700 pp.

Bouchon, M. (1976). Teleseismic body wave radiation from a seismic source in layered medium, *J. Geophys. Res.* **47,** 515–530.

Chen, P. (2005). A unified methodology for seismic waveform analysis and inversion, *Ph.D. Thesis*, University of Southern California, 201 pp.

Chen, P., T. H. Jordan, and L. Zhao (2005). Finite moment tensor of 3 September 2002 Yorba Linda earthquake, *Bull. Seism. Soc. Am.* **95,** 1170–1180.

Dahlen, F. A., S.-H. Hung, and G. Nolet (2000). Fréchet kernels for finite-frequency traveltimes—I. Theory, *Geophys. J. Int.* **141,** 157–174.

Eisner, L., and R. W. Clayton (2001). A reciprocity method for multiple-source simulations, *Bull. Seism. Soc. Am.* **91,** 553–560.

Gaherty, J. B., T. H. Jordan, and L. S. Gee (1996). Seismic structure of the upper mantle in a Central Pacific corridor, *J. Geophys. Res.* **101,** 22,291–22,309.

Gee, L. S., and T. H. Jordan (1992). Generalized seismological data functionals, *Geophys. J. Int.* **111,** 363–390.

Graves, R. W. (1996). Simulating seismic wave propagation in 3D elastic media using staggered-grid finite differences, *Bull. Seism. Soc. Am.* **86,** 1091–1106.

Graves, R. W., and R. W. Clayton (1992). Modeling path effects in 3-dimensional basin structures, *Bull. Seism. Soc. Am.* **82,** 81–103.

Graves, R. W., and D. J. Wald (2001). Resolution analysis of finite fault source inversion using one- and three-dimensional Green's Functions, 1. Strong motions, *J. Geophys. Res.* **106,** 8745–8766.

Hardebeck, J. L., and P. M. Shearer (2002). A new method for determining first-motion focal mechanisms, *Bull. Seism. Soc. Am.* **92,** 2264–2276.

Harvard Seismology (2006). Centroid Moment Tensor (CMT) catalog search, www.seismology.harvard.edu/ (last accessed October 2005).

Hauksson, E. (2000). Crustal structure and seismicity distribution adjacent to the Pacific and North America plate boundary in southern California, *J. Geophys. Res.* **105,** 13,875–13,903.

Hung, S.-H., F. A. Dahlen, and G. Nolet (2000). Wavefront healing: a banana-doughnut perspective, *Geophys. J. Int.* **146,** 289–312.

Katzman, R., L. Zhao, and T. H. Jordan (1998). High-resolution, two-dimensional vertical tomography of the central Pacific mantle using *ScS* reverberations and frequency-dependent travel times, *J. Geophys. Res.* **103,** 17,933–17,971.

Kikuchi, M., and H. Kanamori (1991). Inversion of complex body waves—III, *Bull. Seism. Soc. Am.* **81,** 2335–2350.

Kohler, M. D., H. Magistrale, and R. W. Clayton (2003). Mantle heterogeneities and the SCEC reference three-dimensional seismic velocity model version 3, *Bull. Seism. Soc. Am.* **93,** 757–774.

Komatitsch, D., Q.-Y. Liu, J. Tromp, P. Süss, C. Stidham, and J. H. Shaw (2004). Simulations of ground motion in the Los Angeles basin based upon the spectral-element method, *Bull. Seism. Soc. Am.* **94,** 187–206.

Li, X.-D., and T. Tanimoto (1993). Waveforms of long-period body waves in slightly aspherical Earth model, *Geophys. J. Int.* **112,** 92–102.

Liu, Q.-Y., J. Polet, D. Komatitcsh, and J. Tromp (2004). Spectral-element moment tensor inversions for earthquakes in Southern California, *Bull. Seism. Soc. Am.* **94,** 1748–1761.

Magistrale, H., S. Day, R. W. Clayton, and R. Graves (2000). The SCEC Southern California reference three-dimensional seismic velocity model Version 2, *Bull. Seism. Soc. Am.* **90,** S65–S76.

McGuire, J. J., L. Zhao, and T. H. Jordan (2001). Teleseismic inversion for

the second-degree moments of earthquakes, *Geophys. J. Int.* **145,** 661–678.

Olsen, K. B. (1994). Simulation of three-dimensional wave propagation in the Salt Lake Basin, *Ph.D. Thesis*, University of Utah, Salt Lake City, Utah, 157 pp.

Pasyanos, M. E., D. S. Dreger, and B. Romanowicz (1996). Towards real-time determination of regional moment tensors, *Bull. Seism. Soc. Am.* **86,** 1255–1269.

Shearer, P., E. Hauksson, and G. Lin (2005). Southern California hypocenter relocation with waveform cross-correlation, Part 2: Results using source-specific station terms and cluster analysis, *Bull. Seism. Soc. Am.* **95,** 904–915, doi 10.1785/0120040168.

Süss, M. P., and J. H. Shaw (2003). *P*-wave seismic velocity structure derived from sonic logs and industry reflection data in the Los Angeles basin, California, *J. Geophys. Res.* **108,** no. B3, 2170, ESE 13.

Wessel, P., and W. H. F. Smith (1998). New, improved version of the Generic Mapping Tools released, *EOS Trans. AGU* **79,** 579.

Zhao, L., and T. H. Jordan (2006). Structural sensitivities of finite-frequency seismic waves: a full-wave approach, *Geophys. J. Int.* **165,** 981–990, doi 10.111/j.1365-246X.2006.02993.X.

Zhao, L., T. H. Jordan, and C. H. Chapman (2000). Three-dimensional Fréchet differential kernels for seismic delay times, *Geophys. J. Int.* **141,** 558–576.

Zhao, L., T. H. Jordan, K. B. Olsen, and P. Chen (2005). Fréchet kernels for imaging regional earth structure based on three-dimensional reference models, *Bull. Seism. Soc. Am.* **95,** 2066–2080.

Zhou, Y., F. A. Dahlen, and G. Nolet (2004). 3-D sensitivity kernels for surface-wave observables, *Geophys. J. Int.* **158,** 142–168.

Zhu, L., and D. V. Helmberger (1996). Advancement in source estimation techniques using broadband regional seismograms, *Bull. Seism. Soc. Am.* **86,** 1634–1641.

Zhu, L., and H. Kanamori (2000). Moho depth variation in southern California from teleseismic receiver functions, *J. Geophys. Res.* **105,** 2969–2980.

Zhu, L., and L. A. Rivera (2002). A note on the dynamic and static displacements from a point source in multilayered media, *Geophys. J. Int.* **148,** 619–627.

Department of Earth Sciences
University of Southern California
Los Angeles, California 90089-0740
(L.Z., P.C., T.H.J.)

Institute of Earth Sciences
Academia Sinica
Taipei 115, Taiwan
(L.Z.)

Manuscript received 12 December 2005.